PHYSICAL REVIEW FLUIDS **8**, 043901 (2023)

Reactive-infiltration instability in a Hele-Shaw cell influenced by initial aperture and flow rate

Ting Wang,[1,2,3] Ran Hu,[1,2,*] Zhibing Yang,[1,2] Yi-Feng Chen,[1,2]
Yanlong Li,[3] and Chuang-Bing Zhou[1,2,4]
[1]*State Key Laboratory of Water Resources and Hydropower Engineering Science,*
Wuhan University, Wuhan 430072, China
[2]*Key Laboratory of Rock Mechanics in Hydraulic Structural Engineering of the Ministry of Education,*
Wuhan University, Wuhan 430072, China
[3]*State Key Laboratory of Eco-Hydraulics in Northwest Arid Region of China, Xi'an University of Technology,*
Xi'an 710048, China
[4]*School of Infrastructure Engineering, Nanchang University, Nanchang 330031, China*

(Received 30 October 2022; accepted 21 March 2023; published 11 April 2023)

Reactive-infiltration instability is an inherent nature of a solid dissolution process in a rock fracture. This instability expands the aperture (spacing) of the fracture inhomogeneously and forms preferential dissolution channels (wormholes). The initial aperture and the flow rate play important roles in reshaping the confined geometry because they modify the interplay between flow and reaction that controls the unstable dissolution processes. Here, we perform dissolution experiments in a Hele-Shaw cell to study how the characteristics and pattern transitions are influenced by the initial aperture and the flow rate. We visualize the transitions of dissolution patterns and show that a large aperture usually needs a larger flow rate to form wormholes. We observe the initiating radius at which the dissolving interface shifts from stable to unstable in wormholes due to the decrease of the flow velocity along the radial direction. In the unstable region, the buoyancy-driven convection rolls etch the solid surface into radial stripes with a characteristic wavelength. Decreasing initial aperture or increasing flow rate would suppress the effect of buoyancy-driven convection on the dissolution. Based on the theoretical analysis, we confirm that the initiating radius and the pattern transition can be well represented by the ratio of invading length in the bulk flow direction to the longitudinal direction. Using this concept, we can theoretically estimate the initiating radius and pattern transitions affected by the initial aperture and the flow rate. Finally, a phase diagram of dissolution patterns is established, exhibiting excellent agreement with our experimental results and the existing works. Our work elucidates the mechanism of the initial aperture control on dissolution morphologies in a Hele-Shaw cell, and it provides a benchmark for the investigation of reactive-infiltration instability for permeable media.

DOI: 10.1103/PhysRevFluids.8.043901

I. INTRODUCTION

An instability in the dissolution front usually appears when a reactive fluid dissolves into a uniform rock fracture, which is often referred to as reactive-infiltration instability [1,2]. This phenomenon widely exists in natural and industrial processes, such as karst formation, the long-term safety of high dams in karst areas [3,4], CO_2 geological storage [5–7], and acid-injection enhanced

---

[*] Corresponding author: whuran@whu.edu.cn

oil recovery [8–10]. As a fracture exposed to reactive flow, the instability of the dissolution front has a significant impact on the evolution of its geometry [11–15], and the permeability can increase by several orders of magnitude [16,17]. Understanding the dissolution front instability in fractures is fundamental to quantifying and predicting the dissolution morphologies and the permeability evolution, thereby optimizing the engineering activities.

The reactive-infiltration instability is an inherent nature of solid dissolution processes, even in a Hele-Shaw cell with constant spacing (aperture). Due to the slight perturbation of geometry in Hele-Shaw cells, the region with relatively larger velocities would enhance the enlargement of the local aperture, and in turn, the increase of the local aperture promotes the transport of the reactive fluid. Such positive feedback continuously amplifies during the flow-dissolution processes and creates dominant migration pathways, also known as wormholes [18–25]. From a physical point of view, this instability is governed by the competition among advection, diffusion, and dissolution at the pore scale, which controls the formation and transition of dissolution patterns at the sample scale. A large number of studies have examined the effects of flow rates [19,26,27], fluid properties [11,28,29], fracture scales [30,31], and gravity [32–36] on the instability. Much less emphasis has been given to the initial aperture. The initial aperture controls the timescale of the fluid transport of the dissolved solid phase from the wall to the main flow channel. It then modifies the interplay among advection, diffusion, and dissolution and consequently affects the dissolution patterns. Xu *et al.* [25] observed more ramified and thinner fingers when the initial aperture of a radial gypsum Hele-Shaw cell decreased from 150 to 50 μm. Osselin *et al.* [37] showed that the wavelength of wormholes increases with the amplification of the initial aperture in their microfluidic reactive flow experiments. Despite the above-mentioned achievements, experimental observation and theoretical quantification for the dissolution patterns influenced by the initial aperture are lacking.

It is challenging to theoretically predict the dissolution patterns due to the interplay of advection-diffusion-dissolution in a flow-dissolution system [38]. Generally, governed by this interplay, the dissolution process would form various patterns from face to wormholes to uniform patterns [16,39–42]. Although this interplay can be quantified by the Péclet number Pe and the Damköhler number Da (or the Kinetic number Ki), the threshold Pe and Da (or Ki) for the transition of dissolution patterns are not constant, depending on the flow geometry. In the classic phase diagram for a simple capillary tube proposed by Daccord *et al.* [18], the threshold values of Pe and Da for the transitions from compact to wormholes and to uniform patterns are $\mathrm{Pe} = 1$ and $\mathrm{Da} = 1$, respectively. However, for a porous media packed with NaCl, Golfier *et al.* [19] reported that the transition from face patterns to wormhole patterns occurs at the threshold value of $\mathrm{Pe} = 2 \times 10^{-3}$. Therefore, many researchers employ an alternative parameter, that is, the characteristic length for the development of the dissolution channels, to identify the dissolution patterns [20,43]. Kalia and Balakotaiah [44] reported that the wormhole patterns occur when the ratio of the radial and transverse characteristics lengths is in the range of 0.1 and 1. Starchenko and Ladd [30] reported that uniform patterns are dominant when the characteristic length in the flow direction is larger than the system size. Wang *et al.* [43] have shown that this characteristic length is suitable to quantify the effect of dissolution kinetics on dissolution patterns and thereby establish a phase diagram. The phase diagram for the dissolution patterns that quantifies the effects of the initial aperture and the flow rate, however, has not been reported.

Here, we conduct a series of flow-through dissolution experiments in a transparent, soluble Hele-Shaw cell to investigate the effect of the initial aperture and flow rate on the dissolution patterns. We visualize distinct dissolution patterns from the face, wormholes to uniform. We observe and characterize the initiating radius in a radial Hele-Shaw cell where the reactive-infiltration instability occurs. Based on the analysis of the invading lengths in the flow and transverse directions, we derive an equation to estimate the transitions of these dissolution patterns at different Pe numbers. A phase diagram predicted by this model is presented in the Ki-Pe plane, and the diagram is evaluated by a number of experimental and simulation results. This work provides a fundamental understanding of the influence of aperture on dissolution morphologies, which is of practical significance in the management of reactive flow in geological systems.

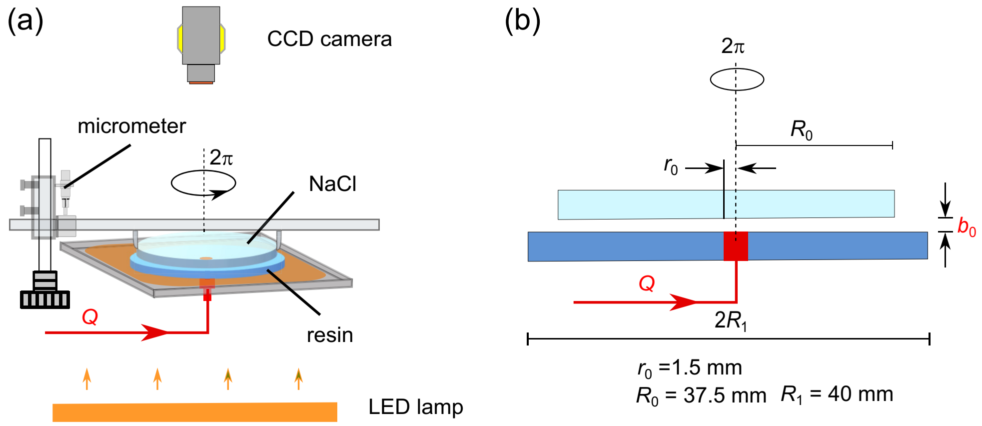

FIG. 1. The flow-dissolution visualization experimental setup. (a) The soluble Hele-Shaw cell is composed of two disks. The upper disk is a NaCl crystal with a smooth surface with $R_0 = 37.5$ mm, and the lower disk is a transparent smooth PMMA surface with $R_1 = 40$ mm. A CCD camera installed above the flow cell records the dissolution process. The space between the two disks, denoted by the initial aperture b_0, is accurately set as 0.3, 0.5, and 0.7 mm by a micrometer installed in the setup. (b) An undersaturated sodium chloride brine is injected into the void space through the central hole of the lower disk with $r_0 = 1.5$ mm with a constant flow rate of Q.

II. MATERIALS AND METHODS

We perform flow-through dissolution experiments in soluble Hele-Shaw cells with various initial apertures using a flow-visualization setup [Fig. 1(a)]. It is an improvement on our previous system [45–47]. The experimental setup consists of a soluble fracture, a syringe pump (PhD Ultra 70-3007, Harvard Apparatus), and an imaging system. The soluble Hele-Shaw cell is composed of a flat PMMA plate and a smooth soluble NaCl crystal, as shown in Fig. 1(b). To stabilize the pressure at the outlet, the PMMA plate with a radius of 40 mm is placed under the NaCl crystal with a radius of 37.5 mm. An inlet is a hole drilled in the center of the PMMA plate with a radius of 1.5 mm. A micrometer is installed in the setup [Fig. 1(a)] to accurately control the initial aperture of the cell. In the imaging system, a CCD camera (Manta G-1236, AVT) was installed over the Hele-Shaw cell to capture the light intensity field transmitted through the fracture cell from the LED light source installed below the fracture [see Fig. 1(a)]. The CCD camera provides an array of 1800 × 1800 pixels for each image. The temperature of the experimental system was controlled at 25 ± 0.5 °C.

To conduct a dissolution experiment, we first saturate the cell with saturated brine for 1 h. Then we inject the unsaturated brine with a density of $C = 23.4\%$ into the cell at a constant flow rate Q. The diffusion coefficient of NaCl solution D_m is 1.61×10^{-9} m^2/s [48,49]. The dissolution rate of NaCl is expressed as $R = k(C_s – C)$, where $C_\mathrm{s} = 26.4\%$ is the saturated concentration, and k is the dissolution rate constant. k is estimated as 5.5×10^{-6} m/s according to the result of Simon *et al.* [50]. The unit of k (m/s) represents the receding rate (m/s) when a crystal face with per unit area (m^2) is dissolved in a solution with per unit concentration difference (represented by mass percent concentration, %). To increase the light absorbance of the solution, the unsaturated brine is dyed with 1/16 g/L of Brilliant Blue R (Macklin). During dissolution, the aperture continues to expand, and the transmitted light intensity recorded by the CCD camera decreases. The evolution of the dissolution morphologies is obtained through an image-processing procedure based on the Beer-Lambert law (Appendix).

A total of 27 flow-through dissolution experiments are performed, with the initial aperture b_0 being 0.3, 0.5, and 0.7 mm and the flow rate $Q = 0.01$, 0.025, 0.05, 0.1, 0.5, 1.0, 2.0, 3.0, and

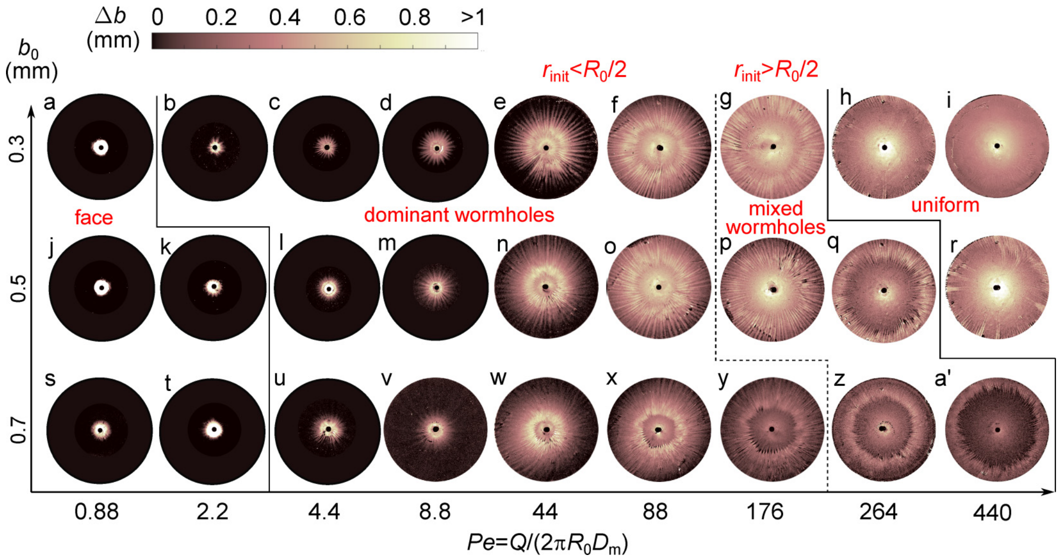

FIG. 2. Observation of the dissolution morphologies under all experimental conditions at the time of the average aperture growth $\langle \Delta b \rangle = 0.3\,\mathrm{mm}$. The Pe number (or the flow rate Q) increases from left to right. The initial aperture b_0 increases from the top to the bottom. The lighter color denotes large aperture growth induced by dissolution, whereas the darker color denotes small aperture growth. The dissolution morphologies exhibit face patterns at small Pe (a), (j), (k), (s), and (t), and uniform dissolution patterns at large Pe (h), (i), and (r). Wormholes are observed at the intermediate Pe (b)–(g), (l)–(q), and (u)–(a′). An initiating radius r_{init} is consistently observed in the wormholes with Pe > 10. Based on the initiating radius, wormhole patterns are divided into dominant wormholes if $r_{\mathrm{init}} < 0.5R_0$ and mixed wormholes if $r_{\mathrm{init}} > 0.5R_0$. See the Supplemental Material in Ref. [51].

5.0 mL/min. During injection, the NaCl crystal is dissolved into the fluid flow and causes the density difference between the unsaturated and saturated brine. We characterize the relation of the advection, diffusion, and dissolution effects with the classical Péclet number $\mathrm{Pe} = vb_0/D_{\mathrm{m}}$ and the Kinetic number $\mathrm{Ki} = kb_0/D_{\mathrm{m}}$, where v is the average flow rate in the whole radial cell, $v = Q/(\pi R_0 \langle b_0 \rangle)$. Here, Pe spans three orders of magnitude with $-0.04 \leqslant \log_{10}\mathrm{Pe} \leqslant 2.64$, and Ki changes from 1.025 to 3.478.

III. RESULTS AND DISCUSSION

A. Dissolution morphologies and the initiating radius

Figure 2 presents the dissolution morphologies for all experimental conditions, corresponding to the distributions of the aperture growth Δb at the time of the average aperture growth $\langle \Delta b \rangle = 300\,\mu\mathrm{m}$. Visually, we observe that the dissolution morphologies shift from the face [Figs. 2(a), 2(j), 2(k), 2(s), and 2(t)] to wormholes and to uniform [Figs. 2(h), 2(i), and 2(r)] with the increase of Pe (or flow rate Q). However, our experimental results are different from those in rough fractures [33,43] or in the gypsum Hele-Shaw cells [25,52]. The smooth dissolution fronts are observed for the face patterns in our Hele-Shaw cells, while rough fronts are always formed in the rough-walled fractures [33,43]. This difference highlights the important role of the roughness of the fracture walls that destabilizes the dissolution front. Moreover, we see that the wormhole is central symmetry and looks like "a flower," as shown in Fig. 2(d). These features manifest the reactive-infiltration instability in the solid dissolution processes in a Hele-Shaw cell.

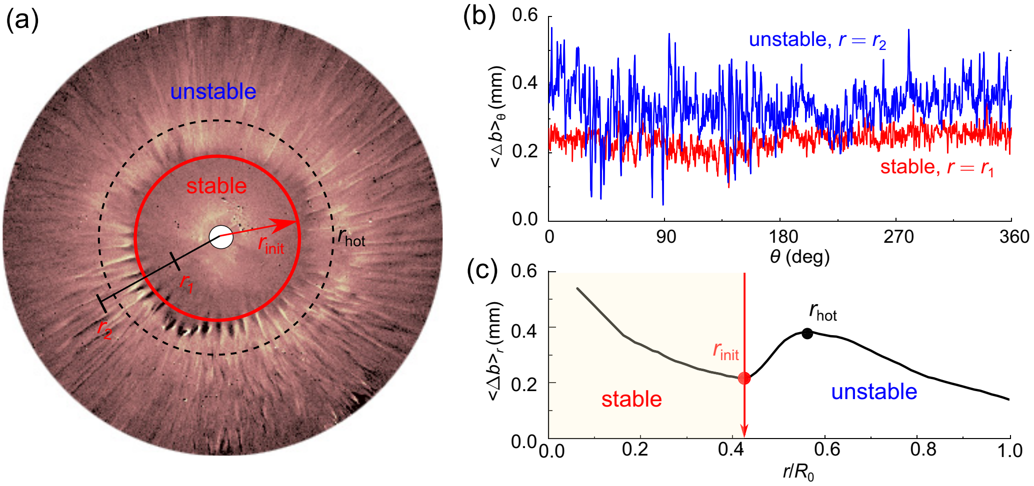

FIG. 3. Quantification of the initiating radius r_{init}. (a) The initiating radius r_{init} is presented for the enlarged image of Fig. 2(f). This radius r_{init} is a critical location where the dissolution front shifts from stable to unstable during a dissolution process. (b) We present the angular aperture growth $\langle \Delta b \rangle_\theta$ at $r = r_1 < r_{\mathrm{init}}$ (in the stable region) and at $r = r_2 > r_{\mathrm{init}}$ (in the unstable region). In the stable region, $\langle \Delta b \rangle_\theta$ has a smaller amplitude, whereas it has a larger amplitude in the unstable region. (c) We also present the radial aperture growth $\langle \Delta b \rangle_r$ to determine r_{init}. It shows that $\langle \Delta b \rangle_r$ reaches its minimum at $r = r_{\mathrm{init}}$, which can be employed to quantitatively locate the initiating radius. We also see that the radial aperture growth $\langle \Delta b \rangle_r$ reaches its maximum at $r = r_{\mathrm{hot}}$ in the unstable region. This point r_{hot} is known as a *dissolution hotspot*, which has been reported and quantified in a previous work [33].

Interestingly, we observe an initiating radius r_{init} in wormholes as $\mathrm{Pe} > 10$. This radius r_{init} is a critical location where the dissolution front shifts from stable to unstable during a dissolution process. As the reactive fluid moves from the inlet $r = r_0$ to the outlet $r = R_0$, the dissolution front is stable for $r < r_{\mathrm{init}}$ and the reactive-infiltration instability occurs as $r > r_{\mathrm{init}}$. This transition of the reactive-infiltration instability in a soluble Hele-Shaw cell is observed in experiments. To get an insight into the initiating radius, we present the angular profiles of average aperture increment $\langle \Delta b \rangle_\theta$ and the radial aperture growth $\langle \Delta b \rangle_r$ at the regions of $r < r_{\mathrm{init}}$ and $r > r_{\mathrm{init}}$ [Figs. 3(b) and 3(c)]. It shows a remarkable difference for the average aperture increment $\langle \Delta b \rangle_\theta$. In the unstable region ($r > r_{\mathrm{init}}$), the curve $\langle \Delta b \rangle_\theta$ displays a larger amplitude with about 0.3 mm [Fig. 3(b)] than that in the stable region ($r < r_{\mathrm{init}}$) with 0.05 mm. Moreover, from Fig. 3(c) we observe that $\langle \Delta b \rangle_r$ reaches its local minimum at this initiating radius, which can be employed to quantitatively determine r_{init}. The radial aperture growth $\langle \Delta b \rangle_r$ decreases with r when $r < r_{\mathrm{init}}$ in the stable region, whereas it would reach its local maximum at $r = r_{\mathrm{hot}}$ in the unstable region ($r > r_{\mathrm{init}}$). This local maximum point, known as a dissolution hotspot, has been observed and quantified in a previous study [33]. The occurrence of the dissolution hotspot is induced by the buoyancy-driven convection (Rayleigh-Taylor instability) in the flow-dissolution system [53,54]. This convection would enhance the local dissolution rate and create radial stripes, as shown in Fig. 3(a). Therefore, it can be concluded that the gravity plays a key role in the unstable region during dissolution, which would be discussed in Sec. III B.

Figure 3(a) further indicates that a smaller value of r_{init} shows a larger area of the region with an unstable dissolution front. Using this feature of r_{init}, we divided the wormhole patterns into two groups: (i) the dominant wormhole patterns if $r_{\mathrm{init}} < R_0/2$ [Figs. 2(b)–2(f), 2(l)–2(o), and 2(u)–2(y)], and (ii) the mixed wormhole patterns for $R_0/2 < r_{\mathrm{init}} < R_0$ [Fig. 2(g), 2(p), 2(q), 2(z), and 2(a′)]. Obviously, if $r_{\mathrm{t}} > R_0$, wormholes disappear, and the front exhibits a uniform pattern

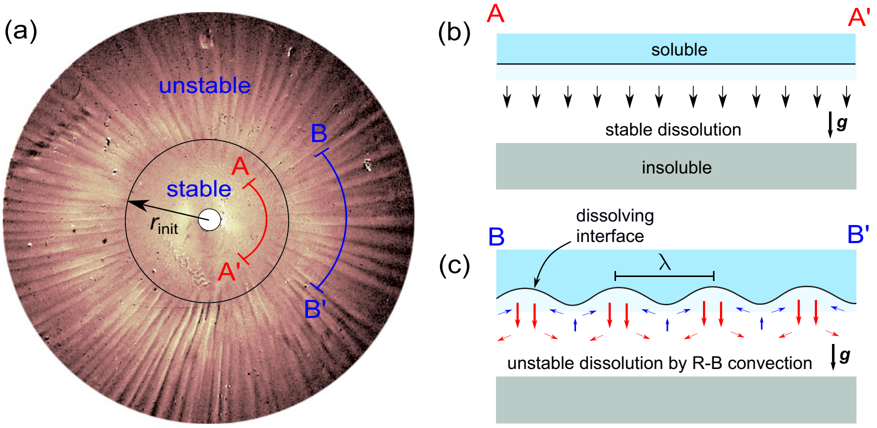

FIG. 4. The mechanism responsible for the initiating radius. (a) We show the cross sections A-A' in the stable region ($r < r_{\text{init}}$) and B-B' in the unstable area ($r > r_{\text{init}}$) for Fig. 2(f). (b) As $r < r_{\text{init}}$, the radial flow rate is so large that the advection in the horizontal direction dominates the dissolution process over the transport in the vertical direction (buoyancy-driven convection). The convection rolls are then highly suppressed, and the Rayleigh-Taylor instability cannot occur. Consequently, the solid phase dissolves uniformly with a stable dissolving interface. (c) As $r > r_{\text{init}}$, the radial flow rate decreases to a state in which the buoyancy-driven convection plays an important role in dissolving the solid phase. The convection rolls due to the buoyancy-driven instability occur, in which the denser solution moves downwards whereas the less dense one moves upwards. This Rayleigh-Taylor instability would enhance the dissolution rate and form an unstable dissolving interface with a characteristic wavelength λ.

[Figs. 2(h), 2(i), and 2(r)]. After identifying dissolution patterns using r_{init}, we then study their transitions affected by the initial aperture b_0. From Fig. 2(a), we see that the critical Pe numbers for these transitions are related to the initial aperture b_0. For a small initial aperture ($b_0 = 0.3$ mm), the critical Pe for the dissolution pattern shifts from face to dominant wormhole at $\text{Pe}_\text{c} \approx 1$, and then from dominant wormhole to mixed wormhole at $\text{Pe}_\text{t} \approx 90$. It further shifts from mixed wormhole to uniform at $\text{Pe}_\text{u} \approx 200$. As the initial aperture increases ($b_0 = 0.7$ mm), these critical Pe numbers also increase, with $\text{Pe}_\text{c} \approx 2$, $\text{Pe}_\text{t} \approx 200$, and $\text{Pe}_\text{u} \approx 400$. These experimental results show that a larger b_0 requires a larger Pe for the formation of the wormhole patterns.

B. Mechanisms responsible for the initiating radius

The initiating radius, as observed in Fig. 3, is related to the interplay between advection in the horizontal direction and the buoyancy-driven convection in the vertical direction. As shown in Fig. 4(a), the radial flow rate $Q/(2\pi r)$ decreases with r in a radial Hele-Shaw cell. As $r < r_{\text{init}}$, the advection of the reactive fluid dominates the process over diffusion and dissolution, and the solid phase dissolves uniformly, producing a stable dissolving interface [Fig. 4(b)]. However, as $r > r_{\text{init}}$, the effect of advection decreases. Due to the density difference in a gravity field, the inflowing fluid would move near the top surface of the cell. The release of the dissolved solid phase forms a denser layer of fluid near the top surface. The denser layer above a less dense layer is a gravitational unstable, resulting in buoyancy-driven convection rolls [Fig. 4(c)]. These convection rolls etch the solid surface into radial stripes with a characteristic wavelength λ.

This phenomenon is also known as a solutal Rayleigh-Taylor instability [34,36,48,49,54–60] and has been investigated under a nonflowing condition [32,34,54]. Under a flowing condition considered in this work, such Rayleigh-Taylor instability can only be observed in the unstable region ($r > r_{\text{init}}$). This is because the buoyancy-driven convection is suppressed by the advection

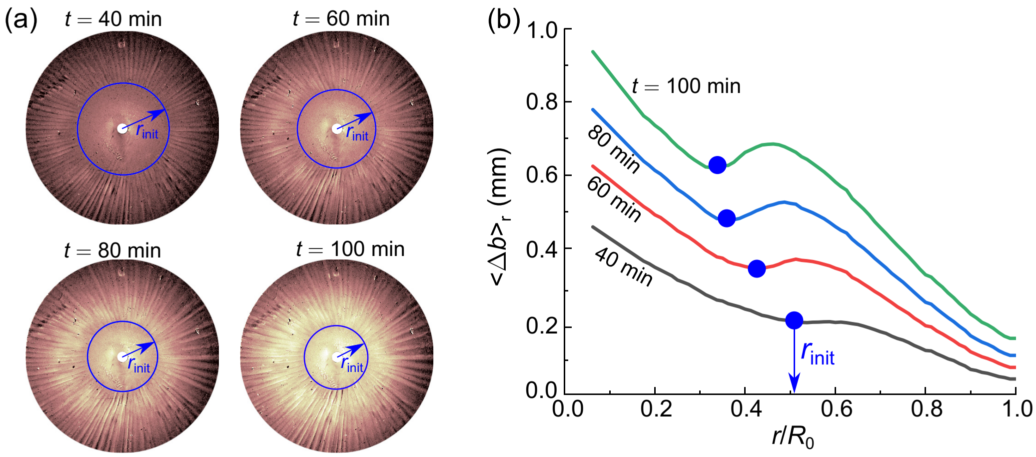

FIG. 5. The evolution of the initiating radius r_{init} during dissolution. (a) We present the evolution of the dissolution patterns of $\text{Pe} = 88$ and $b_0 = 0.3$ mm [Fig. 2(f)] at different dissolution times (40, 60, 80, and 100 min). The corresponding radial profiles of radial aperture growth $\langle \Delta b \rangle_r$ are shown in (b). It shows that r_{init} decreases with time.

and cannot occur in the stable region where the advection effect from the flow rate controls the flow-dissolution system, which has been reported in Ref. [61]. This conclusion can be evidenced by the evolutions of the initiating radius during dissolution [Fig. 5(a)]. As the dissolution proceeds, the aperture increases and thus the advection effect (i.e., radial flow velocity) decreases; the critical radius moves towards the inlet, that is, r_{init} decreases with time [Fig. 5(b)]. This is also supported by the variation of the wavelengths; the details for calculating λ are shown in Fig. 10 in Appendix. As listed in Table I, on the one hand, as the initial aperture b_0 increases (the advection effect decreases), the buoyancy-driven convection is enhanced, creating stripes with a smaller wavelength λ. On the other hand, as Pe increases, the buoyancy-driven convection is suppressed, producing a larger wavelength λ. Previous studies have recognized that the onset of the buoyancy-driven convection would occur if the Rayleigh number Ra exceeds the critical Rayleigh number Ra_c [32,34]. Here, our experiments suggest that the onset of the buoyancy-driven convection may also depend on the advection in the direction orthogonal to convection rolls. The mechanism for the initiating radius in this study also implies that the reactive-infiltration instability in a radial flow geometry is far more complicated than that in a rectangular geometry. For the latter, the flow velocity is independent of the location of the dissolution front, and no transition of the front instability is observed. Similar results are also discussed for multiphase flow problems in a Hele-Shaw cell [62].

TABLE I. The radial wavelengths for the unstable dissolving interfaces at r_{hot}.

Pe / λ (mm) / b_0 (mm)	44	88	176	264	440
0.3	1.32	1.74	1.84	\	\
0.5	1.18	1.14	1.24	1.35	\
0.7	1.14	1.18	1.20	1.22	1.23

C. Theoretical analysis for the initiating radius

As previously indicated, the initiating radius is a critical radius at which the reactive-infiltration instability occurs. This initiating radius reflects the interplay between the advection effect in the horizontal direction and the buoyancy-driven convection in the vertical direction. It has been recognized that the characteristic parameters, such as the onset time and the wavelength, can be estimated by the linear stability analysis for the classic Rayleigh-Taylor instability problems [32,55,56]. However, in this work, for simplicity, we employ the ratio of invading length (γ) in the bulk flow direction (l_{f}) to the longitudinal direction (l_{t}) [44,63], that is, $\gamma = l_{\mathrm{f}}/l_{\mathrm{t}}$, to estimate the initialing radius. This is because this radius r_{init} is an important feature for the wormholes which can be well characterized by γ. Therefore, we expect that the initiating radius r_{init} can be estimated indirectly using γ. To do so, we first estimate γ at the initiating radius r_{init} according to the classical formula [31,43]

$$\gamma_{\mathrm{init}} = \frac{l_{\mathrm{f}}}{l_{\mathrm{t}}} = \frac{2D_{\mathrm{m}}}{v_{\mathrm{init}}}\left[\left(1+\frac{4D_{\mathrm{m}}k_{\mathrm{eff}}}{b_0 v_{\mathrm{init}}^2}\right)^{\frac{1}{2}} - 1\right]^{-1}\left(\frac{D_{\mathrm{m}}b_0}{k_{\mathrm{eff}}}\right)^{-\frac{1}{2}}, \tag{1}$$

where v_{init} can be estimated as $v_{\mathrm{init}} = Q/(2\pi b_0 r_{\mathrm{init}})$; k_{eff} is the effective dissolution rate constant with $k_{\mathrm{eff}} = k/[1 + 2kb_0/(\mathrm{Sh}D_{\mathrm{m}})]$; and Sh is the Sherwood number for one reactive plate, $\mathrm{Sh} \approx 5$ [26].

By Eq. (1), we calculate the invading velocity at the initiating radius, as listed in Appendix, Table II. We find that this parameter γ_{init} remains almost the same with v_{init} [Fig. 6(a)]; it seems to be constant ($\gamma_{\mathrm{init}} = 38$) for all the initiating radii. On this basis, we can predict the initiating radius by substituting $\mathrm{Pe} = Q/(\pi R_0 D_{\mathrm{m}})$ and $v_{\mathrm{init}} = Q/(2\pi b_0 r_{\mathrm{init}})$ into Eq. (1), written as

$$\frac{r_{\mathrm{init}}}{R_0} = \frac{\mathrm{Pe}}{\gamma_{\mathrm{init}}(1+\lambda_{\mathrm{t}}\mathrm{Pe}) - (1+\lambda_{\mathrm{f}}\mathrm{Pe})}\sqrt{\frac{(1+\lambda_{\mathrm{t}}\mathrm{Pe})D_{\mathrm{m}}}{4b_0 k_{\mathrm{eff}}}}, \tag{2}$$

where $\lambda_{\mathrm{t}} = 0.5$, $\lambda_{\mathrm{f}} = 0.1$, and $\gamma_{\mathrm{init}} = 38$ are the constants. It describes the initiating radius as a function of Pe and b_0.

We then evaluate Eq. (2) with the experiment results. As shown in Fig. 6(b), the experiment results with $b_0 = 0.3$, 0.5, and 0.7 mm are denoted by black squares, red circles, and blue triangles. The initiating radius r_{init} predicted by Eq. (2) is shown as black, red, and blue lines, respectively, for $b_0 = 0.3$, 0.5, and 0.7 mm. Obviously, Eq. (2) can reasonably predict the initiating radius r_{init} affected by flow rate (Pe) and initial aperture (b_0). It also captures the transition from the dominant wormholes to the mixed wormholes at $r_{\mathrm{init}} = 0.5R_0$. As the flow rate increases or the initial aperture decreases, the initiating radius shifts toward the outlet. Note that the $\gamma_{\mathrm{init}} = 38$ for the transition from wormhole to uniform in Hele-Shaw cells is larger than that in rough fractures $\gamma = 35$ [43]. This is because the fracture roughness favors the localization of the flow and dissolution channels, leading to a greater difference of the development of the dissolution channels in the two directions. In summary, Eq. (2) provides a mechanistic explanation for the emergence of the initiating radius for the wormholes in Hele-Shaw cells and also allows us to present a model for transitions of dissolution patterns influenced by Pe and b_0 in Sec. III D.

D. Theoretical analysis for the transitions of dissolution patterns

The previous sections have shown that the ratio of invading length γ can well represent the initiating radius observed in the wormholes. Generally, if the ratio of the invading length γ is smaller than a critical value γ_1, wormholes are suppressed, and the face dissolution pattern forms; when the ratio γ is larger than another critical value γ_2, a uniform pattern is produced [23,38,43]. In this section, we use this parameter γ to derive an equation to capture the transition of dissolution patterns observed in Fig. 2, and we show how the initial aperture and flow rate affect the transitions. By

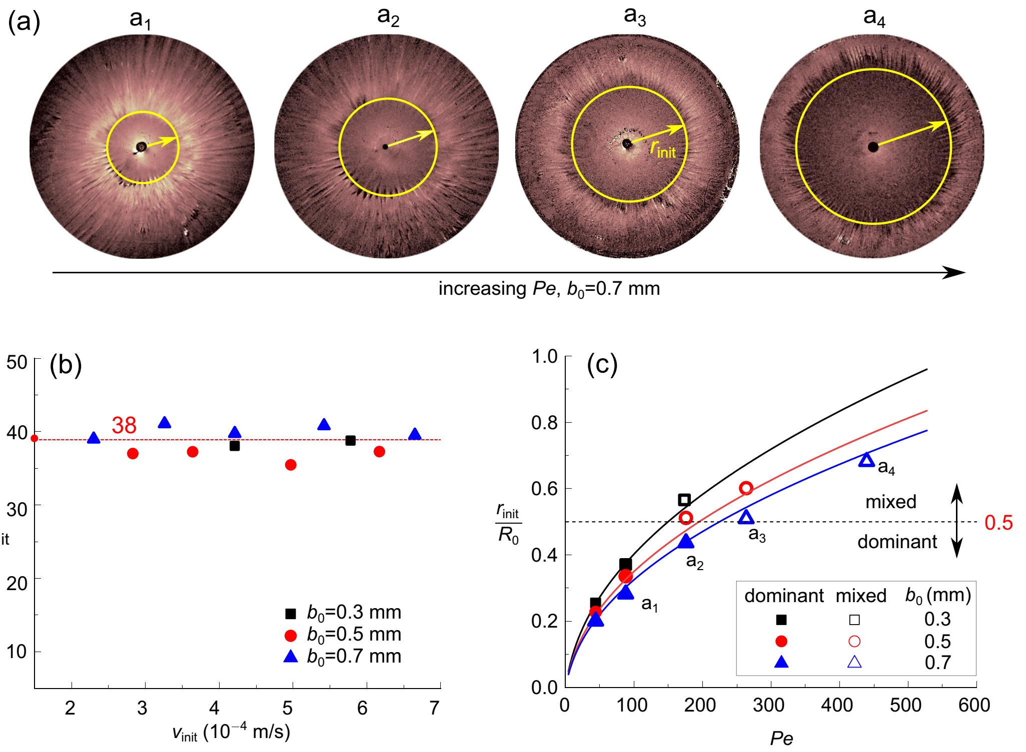

FIG. 6. (a) The effect of flow rate on the initiating radius r_{init}. From observation with $b_0 = 0.7$ mm, r_{init} increases with Pe. (b) Variation of the ratio of invading length γ with the radial velocity at $r = r_{\text{init}}$, i.e., v_{init}. (c) An equation [Eq. (2)] is proposed to estimate the initiating radius r_{init}. The experimental results are denoted as black squares, red circles, and blue triangles for the dissolution with $b_0 = 0.3$, 0.5, and 0.7 mm, respectively. A comparison of the model with the experiments shows good agreement.

substituting the relation $\text{Pe} = Q/(\pi R_0 D_{\text{m}})$ and $k_{\text{eff}} = k/(1 + 2kb_0/\text{Sh}D_{\text{m}})$ into Eq. (1), an equation is obtained for the transitions of dissolution patterns:

$$b_0^{-1} = \frac{[\gamma^2(1+0.1\text{Pe}) - (1+0.5\text{Pe})]^2 \text{Pe}^2 k_{\text{s}}}{\gamma^2(1+0.1\text{Pe})D_{\text{m}}} - \frac{2k_{\text{s}}}{\text{Sh}D_{\text{m}}}. \tag{3a}$$

With $\text{Ki} = kb_0/D_{\text{m}}$, a widely applicable formation for Eq. (3a) can be rewritten as

$$\text{Ki}^{-1} = \frac{[\gamma^2(1+0.1\text{Pe}) - (1+0.5\text{Pe})]^2 \text{Pe}^2}{\gamma^2(1+0.1\text{Pe})} - \frac{2}{\text{Sh}}. \tag{3b}$$

Equation (3) describes the boundary curves for the pattern transition in dissolving Hele-Shaw cells in the Pe-b_0 plane and the Pe-Ki plane, respectively. In these two equations, only one parameter γ needs to be determined.

For the boundary curve of the transition from face to wormhole patterns [the blue line in Fig. 7(a)], the parameter γ_1 can be determined by an average value of two specific points near the boundary of the domains of face and wormhole patterns, that is, $\gamma_1 = 2.5$. Note that this value of the critical γ_1 in the Hele-Shaw cell is smaller than that in rough fractures ($\gamma_1 = 4$), as reported in Wang *et al.* [43]. This is because the fracture roughness would induce irregular flow passages and favor the development of the dissolution channels in the bulk flow direction, i.e., l_{f}, resulting in a larger ratio γ ($\gamma = l_{\text{f}}/l_{\text{t}}$) once the wormholes form.

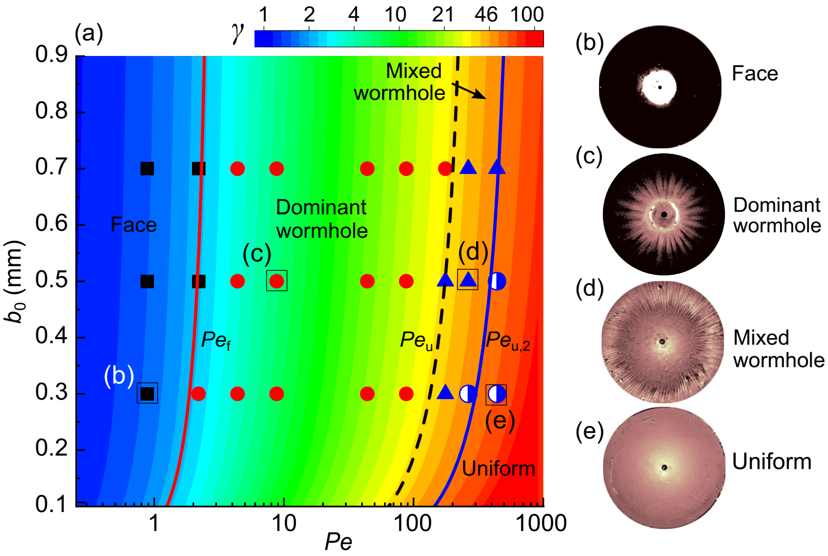

FIG. 7. (a) Phase diagram of dissolution patterns in a Hele-Shaw cell in the Pe-b_0 plane. With the increase of flow rate (Pe), the ratio of invading lengths γ increases, and the forms are from (b) face, to (c) dominant wormhole, to (d) mixed wormhole, and finally to (e) uniform patterns (labeled with an open square). The three curves, estimated by Eqs. (3) and (4), are the boundaries of the regions for the various dissolution patterns. The solid red curve, estimated by Eq. (3a) with $\gamma = \gamma_1 = 2.5$, denotes the transition from face to dominant wormholes. The black dotted curve, estimated by Eq. (3a) with $\gamma = \gamma_2 = 38$, describes the transition from dominant to mixed wormholes. The solid blue curve is estimated by Eq. (4a) with $\gamma = \gamma_2 = 38$, showing the boundary for the transition from mixed wormhole to uniform patterns. The phase diagram is evaluated by experiments from our experimental results denoted by dots (also shown in Fig. 2).

Similarly, parameter γ_2, corresponding to the transition from dominant to mixed wormhole patterns, can be calibrated as $\gamma_2 = 38$ via two specific points near this boundary. As Pe further increases, the dissolution pattern shifts from mixed wormholes to uniform patterns. During this transition, the critical location (or the initiating radius r_{init}) from stable to unstable fronts moves to the outlet. We infer that this r_{init} is larger than R_0 for the uniform pattern. In other words, if the fracture is large enough and the reactive flow retains its aggressivity, wormholes will always occur for radial flow [30,31]. Here, the parameter $\gamma_2 = 38$ is also used for the transition from mixed wormholes to a uniform pattern. However, the Pe number in Eq. (3) should be replaced with the local Pe_{R0} number at the outlet ($r = R_0$, i.e., $\text{Pe}_{R0} = Q/(2\pi R_0 D_{\text{m}}) = \text{Pe}/2$. Therefore, replacing the Pe number with Pe/2, the equation for the transition from mixed wormholes to uniform patterns can be written as

$$b_0^{-1} = \frac{[\gamma^2(2+0.1\text{Pe}) - (2+0.5\text{Pe})]^2 \text{Pe}^2 k_{\text{s}}}{8\gamma^2(2+0.1Pe)D_{\text{m}}} - \frac{2k_{\text{s}}}{\text{Sh}D_{\text{m}}}, \tag{4a}$$

$$\text{Ki}^{-1} = \frac{[\gamma^2(2+0.1\text{Pe}) - (2+0.5\text{Pe})]^2 \text{Pe}^2}{8\gamma^2(2+0.1\text{Pe})} - \frac{2}{\text{Sh}}, \tag{4b}$$

with $\gamma = \gamma_2 = 38$.

We use the experiment results (Fig. 2) to evaluate Eqs. (3) and (4) that capture the pattern transitions. We present a phase diagram of dissolution patterns estimated by Eqs. (3) and (4) in Fig. 7 with three boundary curves in the Pe-b_0 plane. The boundary curves from face to dominant wormholes

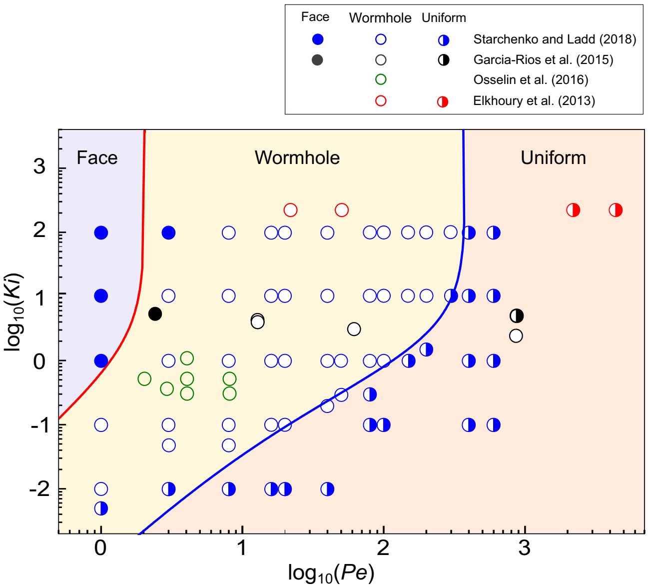

FIG. 8. Evaluation of the phase diagram using the existing experimental results and numerical simulations. The boundary curves for the transition from face to wormholes and from wormholes to uniform patterns are estimated by Eq. (3b) with $\gamma_1 = 2.5$ (red curve) and Eq. (4b) with $\gamma_2 = 38$ (blue curve), respectively. The experimental results conducted by Osselin *et al.* [37] in a gypsum Hele-Shaw cell are located in the right region in this phase diagram. For the numerical simulations that include the face, wormholes, and uniform patterns in a Hele-Shaw cell [30], the phase diagram also well describes the transitions. The experimental results of Elkhoury *et al.* [64] and Garcia-Rios *et al.* [29], including face, wormhole, and uniform patterns, also fall in the right regions of the phase diagram. The reason may be the uneven initial aperture distribution in the experiments. The detailed information for the dissolution patterns in these works is listed in Appendix, Table III.

(the solid red curve) and from dominant to mixed wormholes (the black dot curve) are estimated by Eq. (3) with $\gamma_1 = 2.5$ and $\gamma_2 = 38$, respectively. The value of $\gamma_2 = 38$ is also employed in Eq. (4a) to estimate the boundary curve for the transition from mixed wormhole to uniform patterns (the solid blue curve). The contour plot of γ is given to identify different dissolution patterns. The experiment results, marked by solid squares, circles, triangles, and half-right circles, are also shown in Fig. 7 for comparison purposes. As shown in Fig. 7, we see that the theoretical phase diagram in the Pe-b_0 plane agrees well with experimental results, indicating that Eqs. (3) and (4) reasonably estimate the transitions of dissolution patterns affected by initial aperture and flow rate. The detailed information and the calculations γ of our works are presented in Appendix, Table II.

We further evaluate the phase diagram estimated by Eqs. (3) and (4) using the previous experiments [29,37,64] and simulation results [30]. The phase diagram is presented in the Pe-Ki plane for a broader application (Fig. 8). Since Eqs. (3) and (4) are derived based on the invasion from the flow and transverse directions, they also hold for the linear flow geometry. Note that in the linear flow geometry, the dissolution patterns are related to the flow property at the inlet, therefore v_{init} in Eq. (1) should be the velocity at the inlet.

To obtain the boundary curves, the values of γ_1 and γ_2 should be determined. Here, since the Hele-Shaw cell is also considered in the simulations [30] and experiments [37], the values of $\gamma_1 = 2.5$ and $\gamma_2 = 38$, as given in Fig. 7, are also used in Fig. 8. Previous experiments showed that threshold values are $\gamma_1 = 4.0$ and $\gamma_2 = 35$ for rough fractures, implying that γ_1 and γ_2 can be assumed to be constants. As an approximation, $\gamma_1 = 2.5$ and $\gamma_2 = 38$ are used in the experiments on real carbonate rocks by [29,64]. Therefore, we can present the results in one phase diagram for simplicity. As shown in Fig. 8, the red and blue lines are estimated by Eq. (3b) with $\gamma = \gamma_1 = 2.5$ and Eq. (4b) with $\gamma = \gamma_2 = 38$, respectively. Note that the compact wormholes and necked wormholes in Ref. [30] are collectively classified as wormholes in this work. The dominant and mixed wormholes, shown in Figs. 2 and 7, are also collectively classified as wormholes for simplicity. The detailed information and the calculated γ of these works are presented in Appendix, Table III.

The simulation results from Starchenko and Ladd [30] show the transitions from face to wormholes to uniform patterns. The transitions can be well described by Eqs. (3) and (4). The wormholes observed in the experiments of Osselin *et al.* [37] are also well described by our equations. Two wormholes and two uniform patterns observed in the experiments of Elkhoury *et al.* [64] are both in the right regions predicted by the model. The experiment results on limestone with one face pattern, two wormholes, and one uniform pattern by Garcia-Rios *et al.* [29] fall in the right regions. Only a wormhole pattern is located in the uniform region. This discrepancy may be due to the uneven initial aperture distribution, as discussed by Starchenko and Ladd [30]. It implies that an initial dominant pathway in homogeneous rocks will lead to wormholes rather than uniform or face patterns, as expected. In summary, the good agreement between these results and the phase diagram indicates that Eqs. (3) and (4) are suitable for the prediction of dissolution patterns affected by initial aperture and flow rate with two threshold values ($\gamma_1 = 2.5$ and $\gamma_2 = 38$).

TABLE II. Summary of our experiments in a Hele-Shaw cell.

Exp. no.	Q (mL/min)	$\bar{v} \times 10^4$ (m/s)	b_0 (mm)	Pe	Ki	r_{init}/R_0	r_{hot}/R_0	l_{f} (cm)	l_{t} (cm)	$v_{\text{init}} \times 10^4$ (m/s)	γ_{init}	γ	Dissolution patterns
a	0.01	0.0472	0.3	0.9	1.025	/	/	0.06	0.04	/	/	1.7	face
b	0.025	0.118		2.2		/	/	0.11	0.04	/	/	2.9	dominant
c	0.05	0.236		4.4		/	/	0.20	0.04	/	/	4.8	dominant
d	0.1	0.472		8.8		/	/	0.38	0.05	/	/	7.9	dominant
e	0.5	2.36		44.0		0.28	0.28	1.83	0.08	8.4	39.7	22.4	dominant
f	1	4.72		87.9		0.49	0.48	3.64	0.11	9.6	33.7	33.1	dominant
g	2	9.44		175.8		0.65	0.75	7.27	0.15	14.5	36.8	47.9	mixed
h	3	14.2		263.7		/	/	10.90	0.18	/	/	59.2	uniform
i	5	23.6		439.6		/	/	18.16	0.24	/	/	77.0	uniform
g	0.01	0.0283	0.5	0.9	1.708	/	/	0.09	0.05	/	/	1.6	face
k	0.025	0.0708		2.2		/	/	0.14	0.05	/	/	2.6	face
l	0.05	0.142		4.4		/	/	0.25	0.06	/	/	4.2	dominant
m	0.1	0.283		8.8		/	/	0.46	0.07	/	/	6.8	dominant
n	0.5	1.42		44.0		0.25	0.27	2.19	0.12	5.7	37.6	19.0	dominant
o	1	2.83		87.9		0.37	0.36	4.36	0.16	7.6	37.7	28.1	dominant
p	2	5.66		175.8		0.54	0.55	8.69	0.21	10.5	37.5	40.6	mixed
q	3	8.49		263.7		0.67	0.69	13.02	0.26	12.7	37.4	50.1	mixed
r	5	14.2		439.6		/	/	21.68	0.33	/	/	65.2	uniform
s	0.01	0.0202	0.7	0.9	2.391	/	/	0.11	0.07	/	/	1.6	face
t	0.025	0.0506		2.2		/	/	0.17	0.07	/	/	2.5	face
u	0.05	0.101		4.4		/	/	0.30	0.08	/	/	3.9	dominant
v	0.1	0.202		8.8		/	/	0.54	0.09	/	/	6.3	dominant
w	0.5	1.01		44.0		0.22	0.28	2.55	0.15	4.6	38.9	17.4	dominant
x	1	2.02		87.9		0.31	0.39	5.07	0.20	6.5	41.0	25.6	dominant
y	2	4.04		175.8		0.48	0.56	10.11	0.27	8.4	38.5	37.0	dominant
z	3	6.07		263.7		0.56	0.65	15.14	0.33	10.8	40.7	45.7	mixed
aa	5	10.1		439.6		0.75	0.856	25.21	0.42	13.5	39.6	59.4	mixed

IV. CONCLUSIONS

We combine flow-visualization experiments and theoretical analysis to systematically study the effect of initial aperture and flow rate on the dissolution morphologies and pattern transitions in a radial Hele-Shaw cell. Experimental observations show that the critical Pe numbers corresponding to the transitions of dissolution patterns increase with b_0, implying that a larger aperture needs a larger flow rate to form wormholes. We observe a phenomenon in which the dissolution front shifts from stable to unstable during a dissolution process at the initiating radius. We show that in the unstable region, the buoyancy-driven convection creates radial stripes on the solid surface with a characteristic wavelength. We perform theoretical analysis for the dissolution morphologies and confirm that the ratio of invading lengths in the bulk flow direction to the transverse direction can well characterize the initiating radius and the pattern transitions. On this basis, theoretical estimation is provided. We further propose a phase diagram to predict the transitions of dissolution patterns. Such a phase diagram agrees well with our experiments and also captures the transitions of dissolution patterns reported by the previous experimental and simulation results. Our findings improve the understanding on how reactive-infiltration instability occurs in a dissolution process. The phase diagram for transitions of dissolution patterns is also of significance for many engineering applications, including CO_2 geological storage and enhanced oil recovery.

ACKNOWLEDGMENTS

We acknowledge support from the National Natural Science Foundation of China (No. 52122905), the Basic Science Center Program for Multiphase Media Evolution in Hypergravity of the National Natural Science Foundation of China (No. 51988101), and the National Natural Science Foundation of China (No. 51925906).

TABLE III. A review of flow-through dissolution experimental results in previous works.

Exp. no.	Materials	$\langle b_0 \rangle$ (mm)	$\bar{v} \times 10^4$ (m/s)	Diffusion Coefficient $D_\mathrm{m} \times 10^9$ (m^2/s)	The dissolution rate constant, $k \times 10^4$ (m/s)	Pe	Ki	γ	dissolution patterns	Refs.
A1	calcite	0.3	3.36	2	15	50.4	225.00	9.7	wormhole	[64]
A2			1.46			21.9	225.00	6.2	wormhole	
A3			146			2193.0	225.00	66.9	uniform	
A4			292			4386.0	225.00	94.6	uniform	
B1	calcite	9	6.86	2.5	15	2.5	5.40	2.2	face	[29]
B2		7	46.1			12.3	4.02	6.1	wormhole	
B3		5	291			61.7	3.18	16.8	wormhole	
B4		8	2290			740.7	4.86	54.5	uniform	
B5		6	48.2			12.3	3.84	6.1	wormhole	
B6		4	4520			740.7	2.46	66.7	wormhole	
C1	gypsum	70	/	0.9	0.047	2.9	0.37	4.8	wormhole	[37]
C2		70				4.1	0.37	6.2	wormhole	
C3		70				8.1	0.37	10.6	wormhole	
C4		100				2.0	0.52	3.2	wormhole	
C5		100				4.1	0.52	5.4	wormhole	
C6		100				8.1	0.52	9.1	wormhole	
C7		210				4.1	1.10	4.1	wormhole	

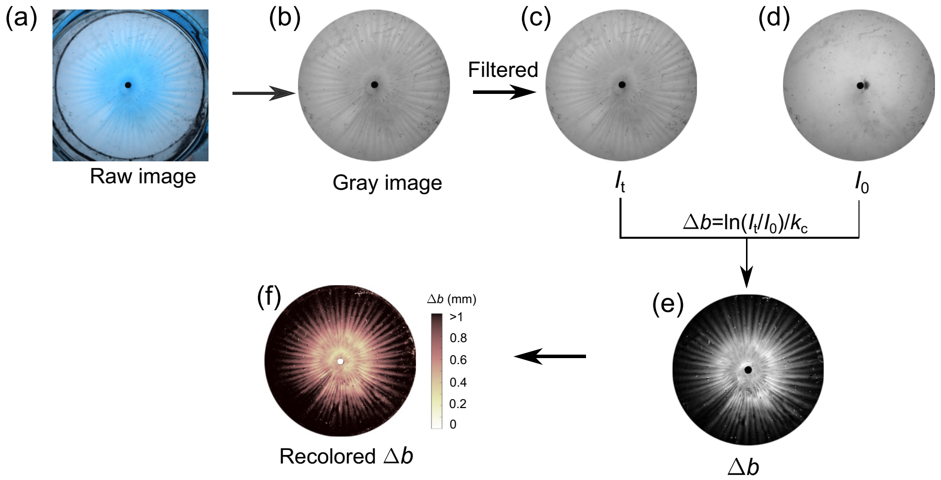

FIG. 9. Image processing procedure. The raw picture (a) obtained by a CCD camera, selected from the experimental results with $\mathrm{Pe} = 44$ and $b_0 = 0.3$ mm [Fig. 2(e)], is cropped to retain the area of interest and remove the useless regions, such as the lateral edges and inlet of the cell by the software PHOTOSHOP. Then, the cropped image is converted to a grey image (b) by the function rgb2grey in MATLAB. Third, the photo is filtered with the function medfilt2 in MATLAB to remove noises. Using the modified Beer-Lambert law [65], the aperture growth Δb (e) can be determined by changes in the transmitted light intensity at the initial state I_0 (d) and the current state I_t (c), i.e., $\Delta b = \ln(I_t/I_0)/k_c$, where k_c is a constant, $k_c = 200$ [43]. Finally, the aperture growth Δb is recolored from dark to light (f).

APPENDIX: DETAILS OF THE FLOW-THROUGH EXPERIMENTS

Detailed information about our experiment and the existing works are shown in Tables II and III. In these tables, the numbers of Pe, Ki, γ for the experiments and their class of dissolution patterns

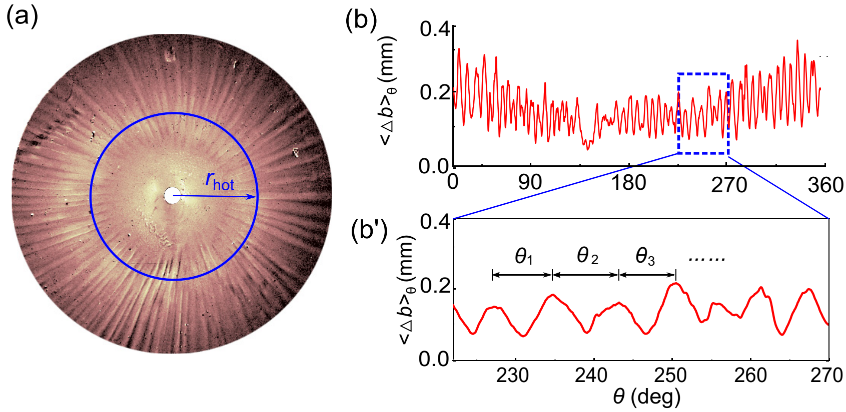

FIG. 10. The determination of wavelength λ for the radial stripes observed in the unstable region. We first present the angular profiles of average aperture growth $\langle\Delta b\rangle_\theta$ at r_{hot} when the average aperture growth $\langle\Delta b\rangle = 0.3$ mm (b), and for that the dissolution reached its local maximum at r_{hot} and the waves developed adequately at this time. The curve $\langle\Delta b\rangle_\theta$ exhibits continuous waves and many peaks. From the enlarged figure of part of $\langle\Delta b\rangle_\theta$ (b′), the wavelength λ_i can be calculated as $\lambda_i = r_{\mathrm{hot}}\pi\theta_i/180$, where θ_i is the spanning angle between two neighboring peaks. Finally, the wavelength is calculated as $\lambda = \sum_1^{n-1}\lambda_i/(n-1)$, where n is the total number of peaks for all of the radial stripes at $r = r_{\mathrm{hot}}$. Detailed information about r_{hot} when $\langle\Delta b\rangle = 0.3$ mm is presented in Table II.

are given. In addition, γ_{init}, r_{init}/R_0 of the initiating radius are also presented. The image processing procedure to obtain Δb is shown in Fig. 9. First, we cropped a raw picture (a) obtained by a CCD camera, i.e., the experiment results with $\mathrm{Pe} = 44$ and $b_0 = 0.3\,\mathrm{mm}$ [Fig. 2(e)], to retain the area of interest by removing useless areas by the software PHOTOSHOP. Then, we converted the cropped image to a grey image (b) by the function rgb2grey in MATLAB. Third, we filtered the photo with the function medfilt2 in MATLAB to remove noises. Finally, we determined the aperture growth Δb (e) using the modified Beer-Lambert law [65] by comparing the changes in the transmitted light intensity at the initial state I_0 (d) and the current state I_{t} (c), i.e., $\Delta b = \ln(I_{\mathrm{t}}/I_0)/k_{\mathrm{c}}$, where k_{c} is a constant, $k_{\mathrm{c}} = 200$ [43]. The aperture growth Δb is recolored from light to dark (f).

Finally, Fig. 10 illustrates a determination of wavelength λ for the radial stripes observed in the unstable region.

[1] P. Ortoleva, E. Merino, C. Moore, and J. Chadam, Geochemical self-organization I; Reaction-transport feedbacks and modeling approach, Am. J. Sci. **287**, 979 (1987).

[2] F. Renard, J.-P. Gratier, P. Ortoleva, E. Brosse, and B. Bazin, Self-organization during reactive fluid flow in a porous medium, Geophys. Res. Lett. **25**, 385 (1998).

[3] A. Hartmann and A. Baker, Modelling Karst Vadose zone hydrology and its relevance for paleoclimate reconstruction, Earth-Sci. Rev. **172**, 178 (2017).

[4] G. Kaufmann and J. Braun, Karst aquifer evolution in fractured, porous rocks, Water Resour. Res. **36**, 1381 (2000).

[5] C. Noiriel and D. Daval, Pore-scale geochemical reactivity associated with CO_2 storage: New frontiers at the fluid-solid interface, Acc. Chem. Res. **50**, 759 (2017).

[6] F. M. Orr, Onshore geologic storage of CO_2, Science **325**, 1656 (2009).

[7] T. Xu, H. Tian, H. Zhu, and J. Cai, China actively promotes CO_2 capture, utilization and storage research to achieve carbon peak and carbon neutrality, Adv. Geo-Energy Res. **6**, 1 (2022).

[8] J. Han, S. Han, D. H. Kang, Y. Kim, J. Lee, and Y. Lee, Application of digital rock physics using X-ray CT for study on alteration of macropore properties by CO_2 EOR in a carbonate oil reservoir, J. Petrol. Sci. Eng. **189**, 107009 (2020).

[9] A. Vengosh, R. B. Jackson, N. Warner, T. H. Darrah, and A. Kondash, A critical review of the risks to water resources from unconventional shale gas development and hydraulic fracturing in the United States, Environ. Sci. Technol. **48**, 8334 (2014).

[10] S. Kiani, S. Jafari, S. N. Apourvari, and H. Mehrjoo, Simulation study of wormhole formation and propagation during matrix acidizing of carbonate reservoirs using a novel in-situ generated hydrochloric Acid, Adv. Geo-Energy Res. **5**, 64 (2021).

[11] W. Li, J. T. Germaine, and H. H. Einstein, A three-dimensional study of wormhole formation in a porous medium: Wormhole length scaling and a Rankine ovoid model, Water Resour. Res. **58**, e2021WR030627 (2022).

[12] N. Qi, G. Chen, C. Liang, T. Guo, G. Liu, and K. Zhang, Numerical simulation and analysis of the influence of fracture geometry on wormhole propagation in carbonate reservoirs, Chem. Eng. Sci. **198**, 124 (2019).

[13] J. Snippe, R. Gdanski, and H. Ott, Multiphase modelling of wormhole formation in carbonates by the injection of CO_2, Energy Proc. **114**, 2972 (2017).

[14] L. Zhang, J. He, H. Wang, Z. Li, F. Zhou, and J. Mou, Experimental investigation on wormhole propagation during foamed-VES acidizing, J. Petrol. Sci. Eng. **198**, 108139 (2021).

[15] C.-X. Zhou, R. Hu, H.-W. Li, Z. Yang, and Y.-F. Chen, Pore-scale visualization and quantification of dissolution in microfluidic rough channels, Water Resour. Res. **58**, e2022WR032255 (2022).

[16] Z. Tian and J. Wang, Lattice Boltzmann simulation of dissolution-induced changes in permeability and porosity in 3D CO_2 reactive transport, J. Hydrol. **557**, 276 (2018).

[17] L. Wang and M. B. Cardenas, Linear permeability evolution of expanding conduits due to feedback between flow and fast phase change, Geophys. Res. Lett. **44**, 4116 (2017).

[18] G. Daccord, R. Lenormand, and O. Liétard, Chemical dissolution of a porous medium by a reactive fluid.—I. Model for the "wormhole" phenomenon, Chem. Eng. Sci. **48**, 169 (1993).

[19] F. Golfier, C. Zarcone, B. Bazin, R. Lenormand, D. Lasseux, and M. Quintard, On the ability of a Darcy-scale model to capture wormhole formation during the dissolution of a porous medium, J. Fluid Mech. **457**, 213 (2002).

[20] P. Grodzki and P. Szymczak, Reactive-infiltration instability in radial geometry: From dissolution fingers to star patterns, Phys. Rev. E **100**, 033108 (2019).

[21] R. Roded, X. Paredes, and R. Holtzman, Reactive transport under stress: Permeability evolution in deformable porous media, Earth Planet. Sci. Lett. **493**, 198 (2018).

[22] P. Szymczak and Anthony J. C. Ladd, The initial stages of cave formation: Beyond the one-dimensional paradigm, Earth Planet. Sci. Lett. **301**, 424 (2011).

[23] P. Szymczak and A. J. C. Ladd, Reactive-infiltration instabilities in rocks. Fracture dissolution, J. Fluid Mech. **702**, 239 (2012).

[24] V. K. Upadhyay, P. Szymczak, and A. J. C. Ladd, Initial conditions or emergence: What determines dissolution patterns in rough fractures?, J. Geophys. Res. **120**, 6102 (2015).

[25] L. Xu, P. Szymczak, R. Toussaint, E. G. Flekkøy, and K. J. Måløy, Dissolution phase diagram in radial geometry, Front. Phys. **8**, 369 (2020).

[26] H. Deng, C. Steefel, S. Molins, and D. DePaolo, Fracture evolution in multimineral systems: The role of mineral composition, flow rate, and fracture aperture heterogeneity, ACS Earth Space Chem. **2**, 112 (2018).

[27] R. L. Detwiler, R. J. Glass, and W. L. Bourcier, Experimental observations of fracture dissolution: The role of Péclet number on evolving aperture variability: Fracture dissolution, Geophys. Res. Lett. **30** (2003).

[28] Y. Al-Khulaifi, Q. Lin, M. J. Blunt, and B. Bijeljic, Reaction rates in chemically heterogeneous rock: coupled impact of structure and flow properties studied by x-ray microtomography, Environ. Sci. Technol. **51**, 4108 (2017).

[29] M. Garcia-Rios, L. Luquot, J. M. Soler, and J. Cama, Influence of the flow rate on dissolution and precipitation features during percolation of CO_2-rich sulfate solutions through fractured limestone samples, Chem. Geol. **414**, 95 (2015).

[30] V. Starchenko and A. J. C. Ladd, The development of wormholes in laboratory-scale fractures: Perspectives from three-dimensional simulations, Water Resour. Res. **54**, 7946 (2018).

[31] P. Szymczak and A. J. C. Ladd, Wormhole formation in dissolving fractures, J. Geophys. Res. **114**, B06203 (2009).

[32] C. Cohen, M. Berhanu, J. Derr, and S. Courrech du Pont, Buoyancy-driven dissolution of inclined blocks: Erosion rate and pattern formation, Phys. Rev. Fluids **5**, 053802 (2020).

[33] R. Hu, T. Wang, Z. Yang, Y. Xiao, Y. Chen, and C. Zhou, Dissolution hotspots in fractures, Geophys. Res. Lett. **48** (2021).

[34] J. Philippi, M. Berhanu, J. Derr, and Sylvain Courrech du Pont, Solutal convection induced by dissolution, Phys. Rev. Fluids **4**, 103801 (2019).

[35] A. Guérin, J. Derr, S. Courrech du Pont, and M. Berhanu, Streamwise Dissolution Patterns Created by a Flowing Water Film, Phys. Rev. Lett. **125**, 194502 (2020).

[36] A. Chaudhuri, H. Rajaram, H. Viswanathan, G. Zyvoloski, and P. Stauffer, Buoyant convection resulting from dissolution and permeability growth in vertical limestone fractures, Geophys. Res. Lett. **36**, L03401 (2009).

[37] F. Osselin, P. Kondratiuk, A. Budek, O. Cybulski, P. Garstecki, and P. Szymczak, Microfluidic observation of the onset of reactive-infiltration instability in an analog fracture, Geophys. Res. Lett. **43**, 6907 (2016).

[38] A. J. C. Ladd and P. Szymczak, Reactive flows in porous media: Challenges in theoretical and numerical methods, Annu. Rev. Chem. Eng. Sci. **12**, 543 (2021).

[39] C. E. Cohen, D. Ding, M. Quintard, and B. Bazin, From pore scale to Wellbore scale: Impact of geometry on wormhole growth in carbonate acidization, Chem. Eng. Sci. **63**, 3088 (2008).

[40] C. N. Fredd and H. S. Fogler, Influence of transport and reaction on wormhole formation in porous media, AIChE J. **44**, 1933 (1998).

[41] Y. Hao, M. Smith, Y. Sholokhova, and S. Carroll, CO_2-induced dissolution of low permeability carbonates. Part II: Numerical modeling of experiments, Adv. Water Resour. Res. **62**, 388 (2013).

[42] Q. Niu and C. Zhang, Permeability prediction in rocks experiencing mineral precipitation and dissolution: A numerical study, Water Resour. Res. **55**, 3107 (2019).

[43] T. Wang, R. Hu, Z. Yang, C. Zhou, Y. Chen, and C. Zhou, Transitions of dissolution patterns in rough fractures, Water Resour. Res. **58**, e2021WR030456 (2022).

[44] N. Kalia and V. Balakotaiah, Modeling and analysis of wormhole formation in reactive dissolution of carbonate rocks, Chem. Eng. Sci. **62**, 919 (2007).

[45] Y.-F. Chen, S. Fang, D.-S. Wu, and R. Hu, Visualizing and quantifying the crossover from capillary fingering to viscous fingering in a rough fracture, Water Resour. Res. **53**, 7756 (2017).

[46] R. Hu, J. Wan, Y. Kim, and T. K. Tokunaga, Wettability effects on supercritical CO_2-brine immiscible displacement during drainage: Pore-scale observation and 3D simulation, Int. J. Greenhouse Gas Con. **60**, 129 (2017).

[47] R. Hu, C. Zhou, D. Wu, Z. Yang, and Y. Chen, Roughness control on multiphase flow in rock fractures, Geophys. Res. Lett. **46**, 12002 (2019).

[48] H. S. Harned and C. L. Hildreth, The differential diffusion coefficients of lithium and sodium chlorides in dilute aqueous solution at 25°, J. Am. Chem. Soc. **73**, 650 (1951).

[49] V. Vitagliano and P. A. Lyons, Diffusion coefficients for aqueous solutions of sodium chloride and barium chloride, J. Am. Chem. Soc. **78**, 1549 (1956).

[50] B. Simon, Dissolution rates of NaCl and KCl in aqueous solution, J. Cryst. Growth **52**, 789 (1981).

[51] See Supplemental Material at http://link.aps.org/supplemental/10.1103/PhysRevFluids.8.043901, movies S1–S4 for the four distinct patterns (face pattern, dominant wormholes, mixed wormholes, and uniform pattern).

[52] G. Daccord, Chemical Dissolution of a Porous Medium by a Reactive Fluid, Phys. Rev. Lett. **58**, 479 (1987).

[53] A. De Wit, Chemo-hydrodynamic patterns and instabilities, Annu. Rev. Fluid Mech. **52**, 531 (2020).

[54] C. Cohen, M. Berhanu, J. Derr, and S. Courrech du Pont, Erosion patterns on dissolving and melting bodies, Phys. Rev. Fluids **1**, 050508 (2016).

[55] M. Berhanu, J. Philippi, S. Courrech du Pont, and J. Derr, Solutal convection instability caused by dissolution, Phys. Fluids **33**, 076604 (2021).

[56] S. Alqatari, T. E. Videbæk, S. R. Nagel, A. E. Hosoi, and I. Bischofberger, Confinement-induced stabilization of the Rayleigh-Taylor instability and transition to the unconfined limit, Sci. Adv. **6**, eabd6605 (2020).

[57] P. Shukla and A. De Wit, Influence of the Péclet number on reactive viscous fingering, Phys. Rev. Fluids **5**, 014004 (2020).

[58] J. Purseed, B. Favier, L. Duchemin, and E. W. Hester, Bistability in Rayleigh-Bénard convection with a melting boundary, Phys. Rev. Fluids **5**, 023501 (2020).

[59] M. Jotkar, L. Rongy, and A. De Wit, Reactive convective dissolution with differential diffusivities: Nonlinear simulations of onset times and asymptotic fluxes, Phys. Rev. Fluids **5**, 104502 (2020).

[60] C. Thomas, S. Dehaeck, and A. De Wit, Effect of precipitation mineralization reactions on convective dissolution of CO_2: An experimental study, Phys. Rev. Fluids **5**, 113505 (2020).

[61] A. Tsinober, R. Rosenzweig, H. Class, R. Helmig, and U. Shavit, The role of mixed convection and hydrodynamic dispersion during CO_2 dissolution in saline aquifers: A numerical study, Water Resour. Res. **58**, e2021WR030494 (2022).

[62] B. Zhao, C. W. MacMinn, and R. Juanes, Wettability control on multiphase flow in patterned microfluidics, Proc. Natl. Acad. Sci. USA **113**, 10251 (2016).

[63] M. K. R. Panga, M. Ziauddin, and V. Balakotaiah, Two-scale continuum model for simulation of wormholes in carbonate acidization, AIChE J. **51**, 3231 (2005).

[64] J. E. Elkhoury, Dissolution and deformation in fractured carbonates caused by flow of CO_2-rich brine under reservoir conditions, Int. J. Greenhouse Gas Con. **16**, S203 (2013).

[65] R. L. Detwiler, S. E. Pringle, and R. J. Glass, Measurement of fracture aperture fields using transmitted light: An evaluation of measurement errors and their influence on simulations of flow and transport through a single fracture, Water Resour. Res. **35**, 2605 (1999).